Aerodynamic effects of forward blade skew in axial flow rotors of controlled vortex design

J Vad*, **A R A Kwedikha, Cs Horváth, M Balczó, M M Lohász,** and **T Régert**
Department of Fluid Mechanics (DFM), Budapest University of Technology and Economics, Budapest, Hungary

The manuscript was received on 6 February 2007 and was accepted after revision for publication on 11 July 2007.

DOI: 10.1243/09576509JPE420

Abstract: Comparative studies have been carried out on two axial flow fan rotors of controlled vortex design (CVD), at their design flowrate, in order to investigate the effects of circumferential forward skew on blade aerodynamics. The studies were based on computational fluid dynamics (CFD), validated on the basis of global performance and hot wire flow field measurements. The computations indicated that the forward-skewed blade tip modifies the rotor inlet condition along the entire span, due to its protrusion to the relative inlet flow field. This leads to the rearrangement of spanwise blade load distribution, increase of losses along the dominant part of span, and converts the prescribed spanwise blade circulation distribution towards a free vortex flow pattern. Due to the above, reduction in both total pressure rise and efficiency was established. By moderation of the radial outward flow on the suction side, being especially significant for non-free vortex blading, forward sweep was found to be particularly useful for potential reduction of near-tip loss in CVD rotors. Application of reliable CFD-based design systems was recommended for systematic consideration and control of both load- and loss-modifying effects due to non-radial blade stacking.

Keywords: axial flow turbomachinery, controlled vortex design, forward blade skew, forward blade sweep, circumferential forward skew

1 INTRODUCTION

Rotors of axial flow turbomachines are often of 'controlled vortex' design (CVD) [**1**]. This means that contrarily to the classic free vortex concept prescribing spanwise constant design blade circulation, the circulation – and thus, the Euler work – increases along the dominant part of the blade span in a prescribed manner. CVD guarantees a better utilization of blade sections at higher radii, i.e. it improves their contribution to the rotor performance. By this means, rotors of high specific performance can be realized, i.e. relatively high flow rate and total pressure rise can be obtained even with moderate diameter, blade count, and rotor speed [**2**, **3**]. CVD gives a means also for reduction of hub losses by unloading the blade root [**4**], and offers a potential to avoid highly twisted blades [**5**]. Furthermore, in multi stage machinery, it provides a strategy to realize an appropriate rotor exit flow angle distribution [**1**].

Blade sweep, dihedral, and skew are known as techniques of non-radial blade stacking. A blade has sweep and/or dihedral if the sections of a datum blade of radial stacking line are displaced parallel and/or normal to the chord, respectively [**6**]. A blade is swept forward if the sections of a radially stacked datum blade are shifted parallel to their chord in such a way that a blade section under consideration is upstream of the neighbouring blade section at lower radius [**3**]. A special combination of dihedral and forward sweep is referred to as circumferential forward skew (FSK) [**7**, **8**]. In this case, the datum blade sections are shifted in the circumferential direction, towards the direction of rotation. By this means, the axial extension of the unskewed (USK) datum blading can be retained, the blade mechanics is expected to be more favourable than in the case of forward sweep alone,

**Corresponding author: Department of Fluid Mechanics (DFM), Budapest University of Technology and Economics, Bertalan Lajos u. 4 – 6, Budapest H-1111, Hungary. email: vad@ara.bme.hu*

and the following aerodynamic benefits, dedicated to the incorporated forward sweep, can be utilized.

The open literature suggests a general consensus that forward sweep/skew gives potential for the following advantages in the part load operational range (flow rates lower than design): improvement of efficiency, increase of total pressure peak, and extension of stall-free operating range by improving the stall margin [**3**, **7**–**12**]. Nevertheless, the research results are rather diversified regarding the judgment of performance and loss modifying effects of forward sweep/skew at flow rates near the design point. In reference [**6**], it is pointed out generally that forward sweep near the tip, i.e. 'positive sweep', gives a potential for reduction of near-tip losses. Based on reference [**9**], application of near-tip FSW can be recommended for efficiency improvement over the operational range near the design point [**3**, **7**, **8**], suggest that the application of forward sweep along the entire span is beneficial for loss reduction and performance improvement. However, forward sweep reported in references [**10**] and [**11**] and FSK in reference [**4**] were found to cause the deterioration of efficiency near the design point. In reference [**12**], the reduction of efficiency was established for a forward-swept rotor over the dominant part of the entire stall-free operational range. Backward sweep was reported to be optimal in reference [**13**] from the viewpoint of efficiency improvement.

The performance and loss modifying aspects of forward sweep/skew, which are specific to the individual case studies as the above literature overview suggests, are closely related to the three-dimensional (3D) features of the blade passage flow [**12**, **14**, **15**]. Such 3D flow features are especially characteristic for rotors of CVD, due to the spanwise blade circulation gradient and the resultant vorticity shed from the blade [**2**]. Although a number of reports are available on forward-swept and FSK rotors of CVD, e.g. [**4**, **7**–**9**, **16**], no special emphasis is given to simultaneous application of CVD and non-radial blade stacking.

The current paper intends to present a case study contributing to a more comprehensive understanding of aerodynamic effects of FSK, CVD, and their combination, at the design flow rate. For this purpose, two rotors of CVD, an USK and a FSK one, are aimed to be compared qualitatively, by means of computational fluid dynamics (CFD).

2 ROTORS OF CASE STUDY

Rotor FSK under present investigation operates in the open-type low-speed wind tunnel facility of the Hungarian Institute of Agricultural Engineering (IAE), Gödöllő, Hungary. The facility and the related custom-built fan were designed at DFM, and were produced by Ventilation Works Ltd., Hungary in 2004. The components and instrumentation of the facility being relevant to the present study are shown schematically in Fig. 1. The main fan characteristics are summarized in Table 1. Geometrical details of the rotor and outlet guide vane (OGV) blading are specified in Table 2. FSK was applied to the rotor blades in order to extend the stall-free operating range. A virtual image of FSK, obtained from the CFD technique, and a front-view photo are presented in Fig. 2. The rotor and OGV blade sections have C4 profiles [**5**, **17**] of 10 per cent maximum thickness along the entire span, with circular arc camber lines. Results for a constant rotational speed of 416 r/min are reported herein. The Reynolds number, calculated with the blade tip circumferential speed, the tip chord and the kinematical viscosity of air at 20 °C is approximately 1.074×10^6. The Mach number which was computed with the blade tip circumferential velocity and the speed of sound in air at 20 °C is 0.13, and therefore, the flow is considered incompressible.

Rotor FSK was originated from the virtual rotor USK of radial stacking line, by shifting the blade sections of USK in circumferential direction towards the direction of rotation, without making any modifications to the USK blade section geometry and stagger angle distribution. The blade trailing edges (TEs) of both USK and FSK fit to planes normal to the axis of rotation. The skew angle in Table 2 is defined as the angle between radial lines fitted to the TEs of the datum and the shifted blade sections. The skew angle is zero at the hub and increases along the span. By this means, it was intended to avoid any stacking line blend points, for which increased losses may be expected [**11**]. Near the hub, the rotor blade sections

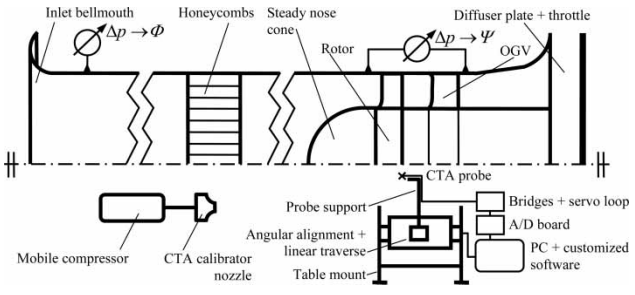

Fig. 1 Experimental facility and instrumentation (the supporting struts for the nose cone and the hub are omitted for simplicity)

Table 1 Main fan characteristics

Casing diameter	2000 mm	Φ_D	0.33
Hub-to-tip ratio ν	0.600	$\Psi_{D\ M\ FSK}$	0.27
Rotor blade count N	12		
OGV blade count	11		
Tip clearance τ	0.036		

Table 2 Fan blading geometry

	Rotor					OGV				
Fraction of span σ	0 hub	0.25	0.50 mid	0.75	1.00 tip	0 hub	0.25	0.50 mid	0.75	1.00 tip
Solidity c/s	1.38	1.01	0.89	0.80	0.72	1.93	1.50	1.32	1.19	1.18
Camber angle (°)	20.3	17.3	16.8	15.8	15.3	60.0	51.5	49.2	47.7	50.1
Stagger angle (°)*	33.9	32.1	30.7	29.9	29.4	57.0	61.7	66.0	68.4	70.0
Skew angle (°)	0.0	0.0	0.3	1.6	3.5					

*Measured from circumferential direction.

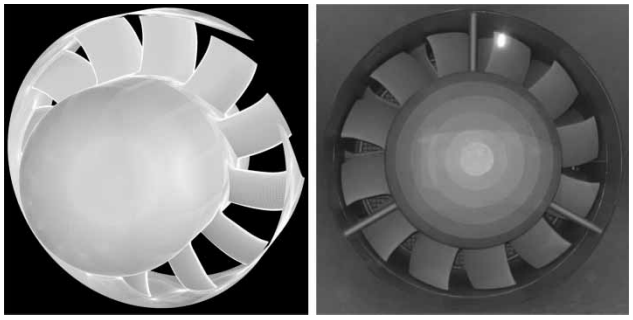

Fig. 2 Virtual axonometric image and front-view photo of FSK

are enlarged. This is favourable from the mechanical point of view, and results in an aerodynamically beneficial positive sweep and positive dihedral [**6**] at the blade root, as potential means of hub loss reduction.

In the following, $\hat{}$ denotes mass-averaging for $\psi_{\mathrm{id}\,2}$, ψ, ω, and φ_{r}, and area-averaging for φ. The USK rotor is of CVD, i.e. the designed blade circulation increases along the span, according to the following power law [**2**, **3**]

$$\hat{\psi}_{\mathrm{id}\,2\mathrm{D}}(R) = \hat{\psi}_{\mathrm{id}\,2\mathrm{D}}(\nu) \cdot \left(\frac{R}{\nu}\right)^{M} \tag{1}$$

The CVD design concept was chosen in order to make possible the preliminary design of each elemental blade cascade along the entire span using the same cascade measurement data basis [**17**], and to reduce blade twist and maintain chord length nearly constant with span, for simplicity in manufacturing.

3 EXPERIMENTS

The experimental facility at IAE is not a test rig dedicated for turbomachinery R&D; the FSK rotor under investigation is its auxiliary unit. Consequently, the facility is in absence of instrumentation expected in turbofan studies. Nevertheless, it had been equipped with an *ad hoc*, on-site measurement setup (Fig. 1), in order to establish an experimental database for validation of the CFD tool.

Characteristic curve and efficiency measurements were carried out on the fan stage. The flow rate was measured using the inlet bellmouth as an inlet cone, calibrated on the basis of detailed velocity measurements made in the test section. The total pressure rise was considered as the difference of static pressures measured downstream of the OGV and upstream of the rotor in the annulus of constant cross-section (equal upstream and downstream dynamic pressures were assumed in the annulus). The differential pressures playing role in the flow rate and total pressure rise measurements were determined using Betz liquid micromanometers. The constancy of rotor speed was checked by means of a laser stroboscope.

The overall efficiency η^* was established as the ratio between aerodynamic performance (product of volume flow rate and total pressure rise) and electric power input to the frequency converter, measured by a clamp meter. Although η^* inevitably includes the losses of the speed control unit, the electric motor, the belt drive, and the bearings, it gives basic qualitative information on the energetic behaviour of the fan.

Detailed flow velocity measurements were carried out at the near-peak-efficiency point of $\Phi = 0.33$, corresponding to the design flowrate. The velocity field was measured using hot wire anemometry, in constant temperature anemometer (CTA) mode, by means of a DANTEC 9055P0511 type cross wire probe connected to DISA 55M type CTA bridges equipped with servo loop. The mobile CTA system is outlined in Fig. 1. v_{x1} as well as v_{x2} and $v_{\mathrm{u}2}$ were measured along the radial span having an axial position of −74.5 and 126.6 per cent midspan axial chord, respectively, where the zero axial position indicates the leading edge (LE) at midspan. The radial traverses were carried out from 0.025 S to 0.975 S, with resolution of 0.025 S. The sampling rate provided 120 measurement readings per blade passage at each radius along the circumference. The measurements were taken at each radial position covering the progress of each blade passage 104 times. For the CTA-based data presented herein, the velocity distributions representing the individual blade passages have been circumferentially averaged.

Table 3 summarizes the pessimistically estimated relative standard uncertainty of the measurement-based quantities presented in the paper, at 95 per cent confidence level, listing the most significant uncertainty sources. The uncertainty analysis has been carried out using the 'root sum square' method, following the methodology in reference [**12**]. Any subvalue

Table 3 Experimental uncertainty

Quantity	Source of uncertainty	U(%)
Φ/Φ_D	Uncertainty of inlet cone calibration	±1.5
	Variation of operating state	±1.0
	Uncertainty of differential pressure measurement	±0.5
Φ/Φ_D	**Overall**	**±2.0**
Ψ/Ψ_D	Variation of operating state	±1.0
	Uncertainty of differential pressure measurement	±0.5
Ψ/Ψ_D	**Overall**	**±1.2**
η^*/η^*_D	Uncertainty of volume flowrate	±2.0
	Uncertainty of total pressure rise	±1.2
	Uncertainty of electric power measurement	±1.0
η^*/η^*_D	**Overall**	**±2.5**
σ	Uncertainty of measurement of endwall relative position	±0.5
$\hat{\varphi}_1, \hat{\varphi}_2, \hat{\psi}_{id}$	Uncertainty of adjusted volume flowrate	±2.0
	Angular misalignment	±2.0
	Temperature and pressure variation	±1.4
	Uncertainty of velocity calibration	±1.4
	Linearization error; voltage signal processing and A/D board resolution limits	±0.7
$\hat{\varphi}_1, \hat{\varphi}_2, \hat{\psi}_{id}$	**Overall**	**±3.5**

of U in the table is not necessarily the error due to the related uncertainty source in itself but the uncertainty propagating due to this error (e.g. the U subvalue specified for the differential pressure measurement for Φ/Φ_D is not the measurement uncertainty of the manometer in itself). The overall uncertainties of the quantities presented herein are taken as the square root of sum of squares of U subvalues. The uncertainty is generally higher than expected in turbomachinery studies [**8**], due to the *ad hoc* measuring technique and to the non-laboratory environmental conditions. The overall measurement uncertainty ranges are indicated by error bars in the diagrams in the vicinity of the measurement data points.

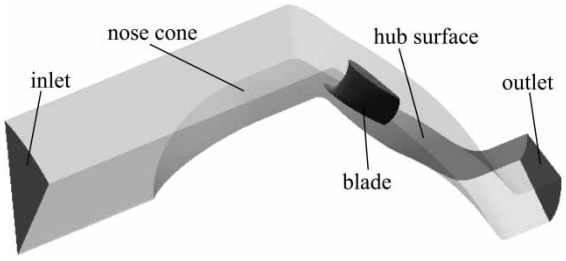

Fig. 3 Computational domain for FSK (the casing is hidden for clarity)

4 CFD TECHNIQUE

The flow fields in USK and FSK were simulated by means of the commercially available finite-volume CFD code FLUENT [**18**]. Referring to references [**7**], [**8**], [**16**], and [**19**] reporting on computations for swept and leaned fan and compressor rotors, the standard $k-\varepsilon$ turbulence model [**20**] has been used. The enhanced wall treatment of FLUENT was applied, incorporating a blended model [**21**] between the two-layer model and the logarithmic law of the wall. Among the two-equation turbulence modelling options built into FLUENT, this technique was found to give the most reasonable agreement with the measurement results presented later.

Taking the periodicity into consideration, the computations regarded one blade pitch only. A typical computational domain is presented in Fig. 3. The domains extend to approximately 8 and 3.5 midspan axial chord lengths upstream and downstream of the rotor blading in the axial direction, respectively. The inlet face is a sector of the circular duct with 30° central angle. Downstream of the inlet face, sectors of the steady inlet cone and the rotating hub with one blade in the middle of the domain are included for both types of blading.

At the inlet face, a swirl-free uniform axial inlet condition corresponding to the actual flow rate has been prescribed. The inlet turbulence intensity has been set to 1 per cent, and the casing diameter was taken as the hydraulic diameter for the calculation of the turbulence length scale. Utilizing the features of the annular cascade configuration, boundary conditions of periodicity were applied. A zero diffusion flux condition has been used for all flow variables at the outlet boundary (outflow condition in FLUENT [**18**]).

Taking [**19**, **22**] as preliminary references, structured hexahedral mesh has been developed for the entire computational domain. This meshing technique is felt promising from the viewpoint of computational accuracy. Furthermore, it offers a means to reduce the computational cost by moderating the cell number.

About 50 per cent of the cells are located in the refined domain in the vicinity of the blade. Taking up the challenge of the relatively complicated blade geometry, due to skew above midspan and LE sweep

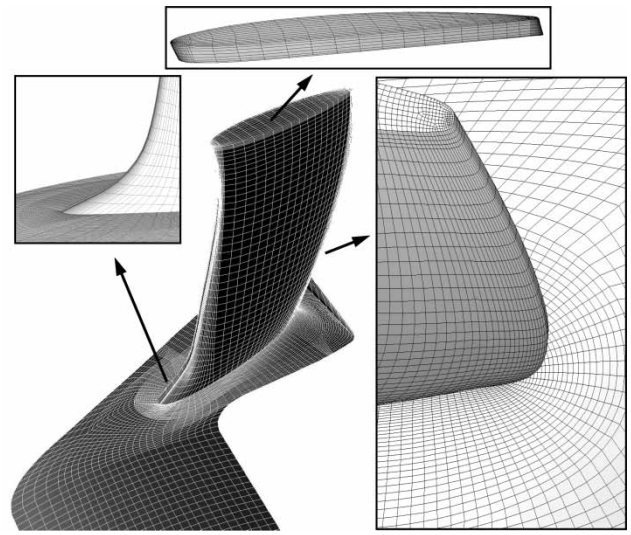

Fig. 4 Finer mesh for FSK near the LE, TE, and tip

near the hub, the domain consists of 31 blocks. Fig. 4 shows representative segments and views of the mesh for FSK near the LE, TE, and tip. An O-type mesh topology has been built around the LE and TE, while H-type topology is applied to the entire rotor blade passage. Figure 5 presents a detail of the mesh topology in the tip clearance region.

The equiangle skewness of a cell is defined as the maximum value of the ratio of actual and possibly highest deviation from the optimum angle, considering each vertex [**18**]. The grid design ensures that 99 per cent of the cells have equiangle skewness less than 0.7, and the maximum skewness value is 0.82. The highest skewness values appear near the LE and TE. Over the dominant part of the SS and PS, the skewness is less than 0.25.

During the computations, the majority of y^+ values fell within the range of 30–100, fulfilling the requirements of the applied wall law. The discretization of the convective momentum and turbulent quantity fluxes were carried out by the Quadratic Upstream Interpolation for Convective Kinematics (QUICK) method.

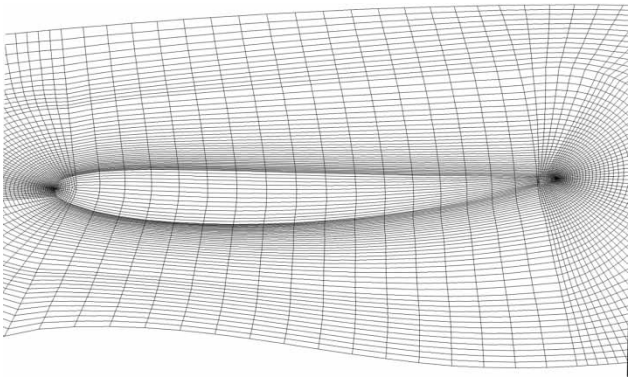

Fig. 5 Mesh topology in the tip clearance region

Typical computations required approximately 3000 iterations. The solutions were considered converged when the scaled residuals [**18**] of all equations were resolved to levels of order of magnitude of 10^{-6}.

4.1 Grid sensitivity studies

Four discretization levels were used for the computation. Taking the 'coarse' mesh consisting of about 204.000 hexahedral cells as a basis, nearly uniform refinement in axial, pitchwise, and spanwise directions resulted in the 'mid', 'finer', and 'finest' meshes (about 301.000, 494.000, and 694.000 cells, respectively). The finer mesh, forming the basis of CFD results presented in the paper, consists of 45 nodes along the span. Clearance meshes resolved in spanwise direction by 5, 9, and 17 nodes were tested, taking the finer mesh as a basis. Application of nine nodes in the clearance was concluded to be necessary, but further refinement was found to be needless for the fidelity of the numerical solution. For the finer mesh, the outer domain (H-mesh) consists of 203, 27, and 54 grid nodes in axial, circumferential, and spanwise directions, respectively.

The ideal total pressure rise was found to be the most sensitive indicator of dependence of the numerical solution on discretization. Figure 6 presents the $\hat{\psi}_{\mathrm{id}\,2}$ data computed for FSK at the design flow rate using the four discretization levels. The grid-independency of results based on the finer mesh is achieved on an acceptable level from the aspect of present studies. The computational data presented from this point onwards are based on the finer mesh numerical results.

4.2 Validation analyses

Figure 7 shows the measured spanwise $\hat{\varphi}_1$, $\hat{\psi}_{\mathrm{id}\,2}$, and $\hat{\varphi}_2$ distributions established on the basis of CTA measurement data for the design point. The experimental data are compared in the figure with the distributions

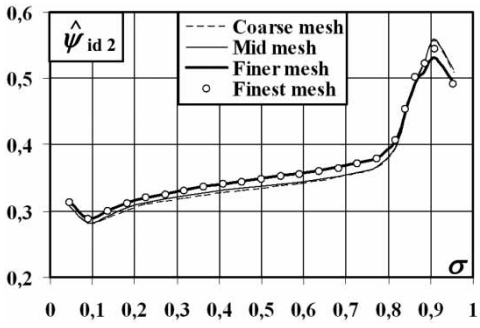

Fig. 6 Influence of overall mesh refinement on the numerical solution

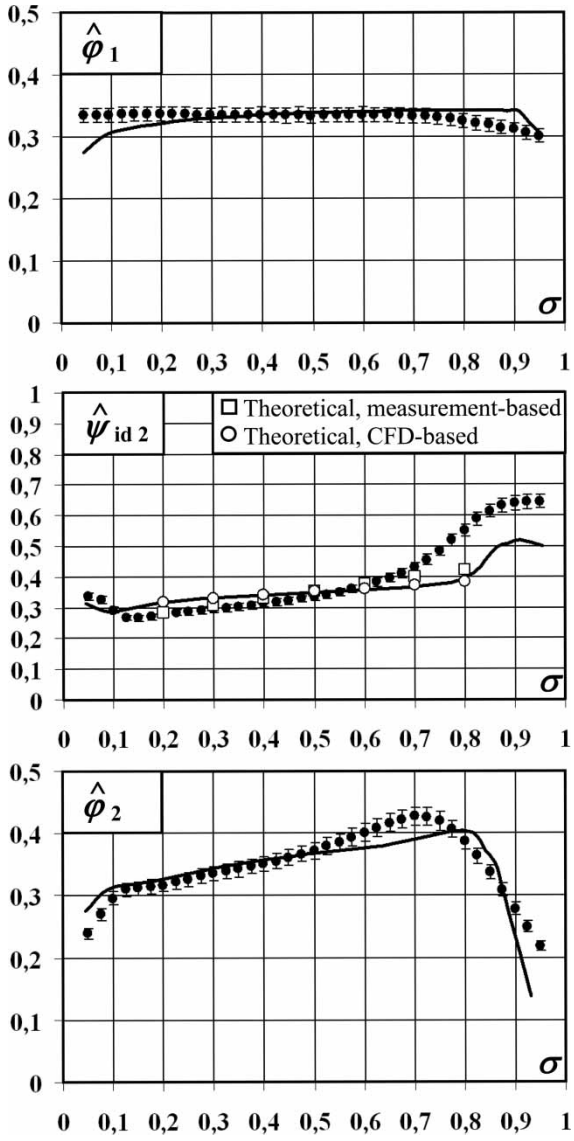

Fig. 7 Measured and computed flow details for FSK. Black dots: measurements, lines: CFD

computed for FSK at the axial positions of the measurements.

The $\hat{\varphi}_1$ diagrams show the approximate realization of the uniform axial rotor inlet condition used in blade design. The computed $\hat{\varphi}_1$ data fall below the measured values near the hub, and the related 'displacement effect' results in increased computed axial velocity above midspan. The discrepancy of the near-hub data is dedicated to the difference between the realized and modelled inlet geometries, with special regard to the inlet cone shape. Although the simulation considers an inlet nose cone with smooth surface, the inlet cone has eventually been assembled from conical segments, as seen in Fig. 2, for manufacturing simplification being accepted for industrial fans. The edges appearing at the connection of the segments act as turbulence generators, refreshing the hub inlet boundary layer otherwise being thickened.

The rotor inlet axial velocity underpredicted by CFD leads to higher flow incidence and blade load (lift) below midspan. Considering nearly unchanged free-stream relative velocity w_∞, the increased blade lift of an elemental cascade leads to increased outlet swirl and ideal total pressure rise, according to the following classic approximate relationship [**5**, **11**, **17**], assuming swirl-free inlet far upstream

$$\frac{c}{s}C_{\mathrm{L}} \approx \frac{2\hat{v}_{\mathrm{u}2}}{\hat{w}_\infty} \tag{2}$$

Just the opposite tendency, i.e. decreased incidence, lift, outlet swirl, and ideal total pressure rise is expected above midspan where the rotor inlet axial velocity is overpredicted in comparison with the measurements. The trends explained above appear in the $\hat{\psi}_{\mathrm{id}\,2}$ plots where the computed data are higher and lower than the measurement-based ones below and above midspan, respectively. The 'theoretical' $\hat{\psi}_{\mathrm{id}\,2}$ distributions specified in Fig. 7, calculated from 20 to 80 per cent span using the model described in Appendix 2, correlate fairly well with the CFD – as well as with the measurement-based $\hat{\psi}_{\mathrm{id}\,2}$ diagrams. This confirms the physical relevance and consistency of both the measured and computed $\hat{\varphi}_1$, $\hat{\psi}_{\mathrm{id}\,2}$, and $\hat{\varphi}_2$ data sets.

Besides the above described incidence effect, another reason for the discrepancies above midspan, especially near the tip, is the limited capability of the applied turbulence model. However, even with the presence of the incidence effect, the relative differences between the computed and measured $\hat{\psi}_{\mathrm{id}\,2}$ and $\hat{\varphi}_2$ data reported here do not exceed, up to 90 per cent span, the maximum differences valid for a representative forward-skewed fan (AV30N fan, 30° FSK) studied in references [**7**] and [**8**] involving standard $k-\varepsilon$ modelling. It should be noted that the validity of the CFD technique in references [**7**] and [**8**] has been accepted for widespread investigation of CVD rotors with non-radial blade stacking.

All of the qualitative features judged to be essential for the validity of the CFD tool on the basis of reference [**3**] – i.e. the overturning (increased $\hat{\psi}_{\mathrm{id}\,2}$) near the rotating hub; the spanwise increase of ideal total pressure rise, fitting to the CVD concept [**2**]; the peak in $\hat{\psi}_{\mathrm{id}\,2}$ near the blade tip due to the presence of high-loss fluid; and the decrease of swirl near the casing due to the underturning effect of the stationary casing wall and the leakage flow – are resolved by the computation.

The validity of the CFD method enables the representation of the following trends observed in the measured $\hat{\varphi}_2$ data: axial velocity reduction near the blade root due to the hub boundary layer; increasing

axial velocity along the dominant part of span, due to the CVD concept [**2**, **16**]; and velocity defect near the casing, due to the presence of high-loss fluid as well as the casing boundary layer and leakage flow. The $\hat{\varphi}_2$ values below midspan and the predicted location and value of maximum axial velocity are in fair agreement with the experiments.

The measured and computed characteristic and efficiency curves are shown in Fig. 8. Ψ_{CFD} has been calculated on the basis of the difference between the computed mass-averaged static pressures at the rotor outlet and inlet CTA measurement locations in the annulus. The total pressure and flow coefficient data are normalized by the corresponding values of the measured FSK design point ($\Psi_{D\,M\,FSK} = 0.27$, $\Phi_D = 0.33$). η_{CFD} was calculated as the product of computed global total pressure rise and volume flow rate data divided by the computed shaft power input. The efficiency data have been normalized by appropriate reference values taken at the design flow rate. Polynomial trend lines have been fitted to the data points in the figure.

The [Φ_D, $\Psi_{D\,M\,FSK}$] design point and the slope of the $\Psi_{M\,FSK}(\Phi)$ curve near the design flow rate are fairly well captured by the simulation. The measured and computed trends of efficiency variance from the design point towards moderately lower flow rates are also in fair agreement.

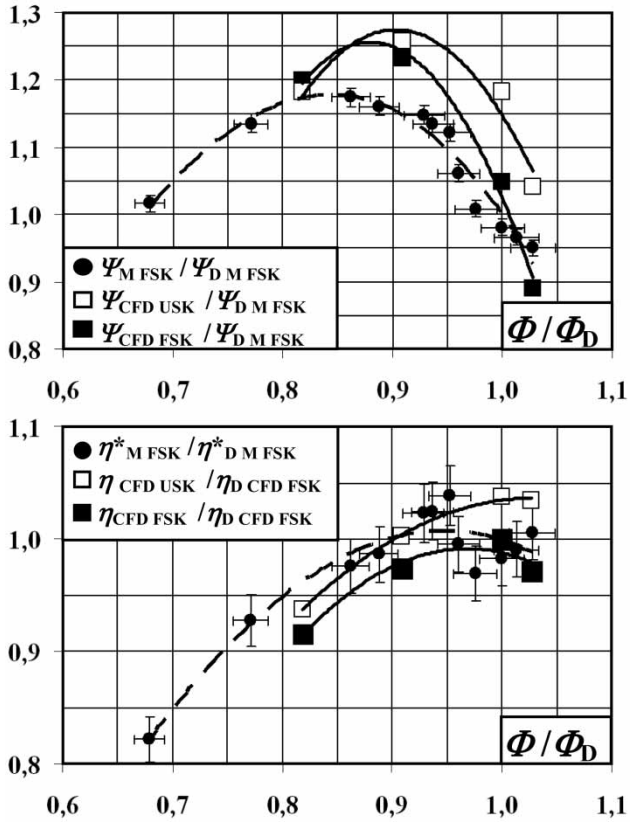

Fig. 8 Measured and computed global performance curves

5 COMPARATIVE SURVEY

5.1 Comparison of USK and FSK performance curves

Figure 8 offers a comparison between the performance curves computed for USK and FSK. Despite the limited capability of the applied turbulence model at lower flow rates, the computed $\Psi(\Phi)$ curves represent the following well-known qualitative features dedicated to forward sweep/skew: (a) if no blade correction is applied for retaining the original Euler work, Ψ is reduced near the design flow rate [**4**, **7**, **8**, **12**, **14**, **16**], (b) the total pressure peak is shifted towards lower flow rates, and (c) Ψ is improved at flow rates considerably lower than the stall margin of the rotor with radially stacked blades [**3**, **11**]. The computed $\eta(\Phi)$ plots show that the deterioration of total efficiency is less drastic for FSK when throttling from the design flowrate.

The total efficiency computed for FSK at the design point falls below the value for USK. This observation, fitting to former experiences in references [**4**] and [**10**–**12**], is the aspect provoking the discussion in the following sections.

5.2 Design flowrate: pitchwise averaged data

Figure 9 presents the spanwise distribution of pitchwise averaged values for the dimensionless rotor inlet and outlet axial velocities as well as radial velocity, ideal total pressure rise, and total pressure loss coefficient at the outlet. The inlet ('1') and outlet ('2') planes have the axial position of −20.0 and 113.0 per cent midspan axial chord, respectively, where the zero axial position indicates the LE at midspan.

As the figure suggests, the applied blade skew has an influence on the rotor inlet flow field: the inlet axial velocity for FSK is increased near the tip and is reduced at lower radii, as can be observed for FSK rotors in reference [**4**]. The outlet axial velocity is increased below midspan for FSK. The difference in radial rearrangement of fluid for USK and FSK, i.e. radially inward dominant flow for FSK [**4**, **7**], is visible on the outlet radial velocity plots. As the ideal total pressure rise and axial velocity plots show, FSK performs increased and decreased Euler work compared to USK below and above midspan, respectively. Such trend appears in reference [**7**] as well (AV30N fan). The Euler work at the tip is reduced due to non-radial blade stacking, as was observed in [**11**].

Figure 9 presents also the $\hat{\psi}_{id\,2D}$ and $\hat{\varphi}_{2D}$ distributions that were determined as outlined in Appendix 2. These distributions indicate the increase of $\hat{\psi}_{id\,2D}$ and

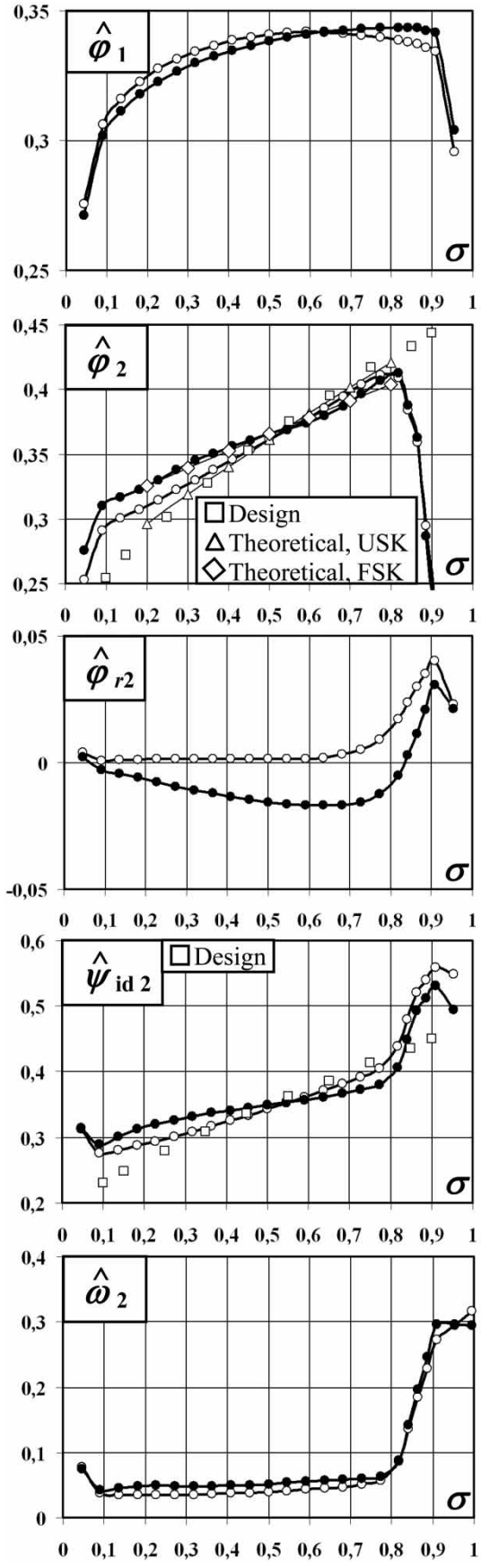

Fig. 9 Pitchwise averaged data. White dots: USK, black dots: FSK

$\hat{\varphi}_{2D}$ along the span due to the CVD concept. They served as a basis for the preliminary design of the rotor blade sections further from the annulus walls. Considering the non-uniformity of CFD-predicted axial rotor inlet condition, which differs from that used in the design concept, the agreement between the design and USK distributions is fair farther from the endwalls. However, increased discrepancy can be observed between the design and FSK distributions.

Although the total pressure loss is reduced near the tip, it is increased over the dominant part of span due to skew. The same tendency was reported in reference [**11**] for a rotor with forward sweep at the tip.

The above tendencies will be explained in the following section, by means of analysis of the detailed flow field. Rotor inlet and outlet flow maps will be presented. Furthermore, the flow field will be surveyed at 20 and 90 per cent span, being two representative locations where significant differences occur in the fluid mechanical behaviour of USK and FSK (Fig. 9).

5.3 Design flowrate: pitchwise resolved data

Figure 10 presents the maps of ideal total pressure rise, axial and radial velocities, and total pressure loss coefficient at the rotor outlet. The regions downstream of the SS and PS, separated by the blade wake zone, are indicated by appropriate labels. These data reflects the trends seen in Fig. 9. For USK, spanwise increase of $\psi_{id\,2}$ dominates along the span, according to the CVD concept based on equation (1). The spanwise gradient of Euler work and blade circulation results in increasing axial velocity along the dominant part of the span according to the physical concept described in Appendix 2, and in vortices shed from the TE. The TE shed vorticity induces radially inward and outward flow on the PS and SS, respectively, as observed also in references [**2**] and [**3**].

Circumferential FSK causes substantial changes in the 3D blade passage flow structure. The spanwise gradient of $\psi_{id\,2}$ is reduced for FSK, for reasons explained later. This trend was observed also in references [**4**] and [**7**]. Based on the physical principle expressed in equation (7) in Appendix 2, the moderation of spanwise $\psi_{id\,2}$ gradient causes the moderation of spanwise variance of φ_2. The theoretical $\hat{\varphi}_2$ plots in Fig. 9, composed as described in Appendix 2, and correlating fairly well with the CFD data, justify this physical trend. The reduction of $d\hat{\varphi}_2/dR$ corresponds to an increase and a decrease of φ_2 below and above midspan, respectively, as was found also in references [**4**] and [**7**–**9**]. According to continuity, this yields the dominance of inward flow in terms of pitchwise averaged radial velocity (negative $\hat{\varphi}_{r2}$ values for FSK in Fig. 9), corresponding to the amplification and the attenuation of radially inward and outward flow on the PS and SS, respectively. The moderation of $d\hat{\psi}_{id\,2}/dR$,

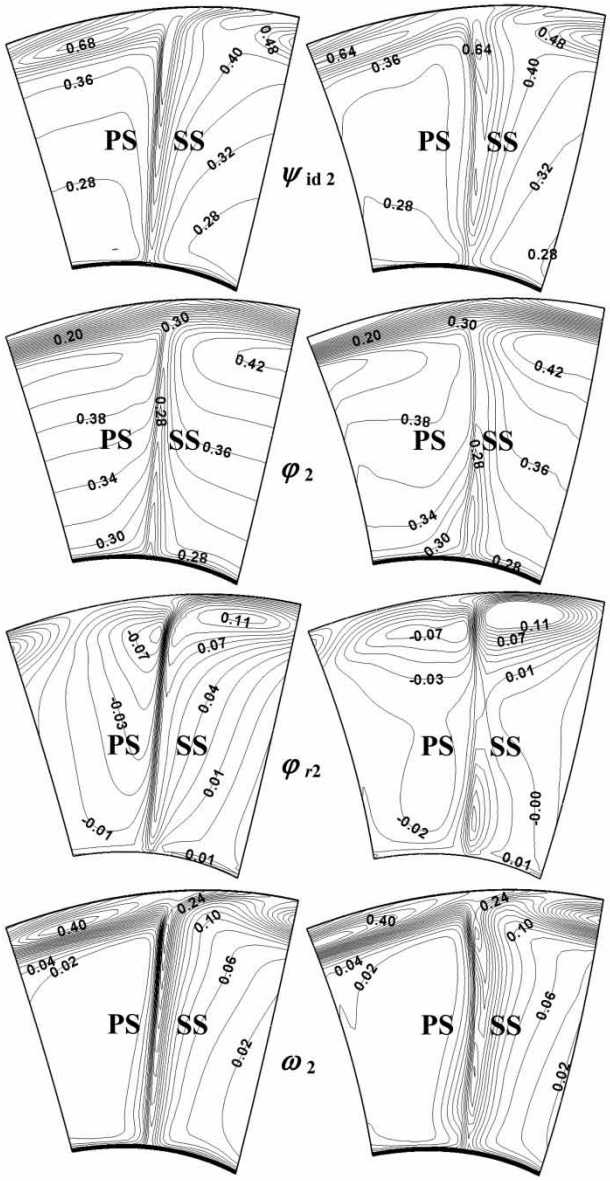

Fig. 10 Outlet flow maps. Left column: USK, right column: FSK

i.e. reduction of spanwise blade circulation gradient, results in the attenuation of TE shed vorticity [**2**, **5**] for FSK, also contributing to the moderation of radial outward flow on the SS.

The mechanism by which FSK attenuates the SS radial outward flow is demonstrated in Fig. 11. Due to FSK, the isobars in the decelerating region are inclined 'more forward' for FSK than for USK. Therefore, the local radial outward flow is moderated, the flow is guided 'more inward' for FSK on the SS. Such radial flow controlling effect has been described qualitatively in reference [**9**].

The moderation of $\mathrm{d}\hat{\psi}_{\mathrm{id}\,2}/\mathrm{d}R$ detected for FSK is explained as follows. Figure 12 shows the axial velocity and ideal total pressure rise maps at the rotor inlet. The upstream regions where the forward effect of SS

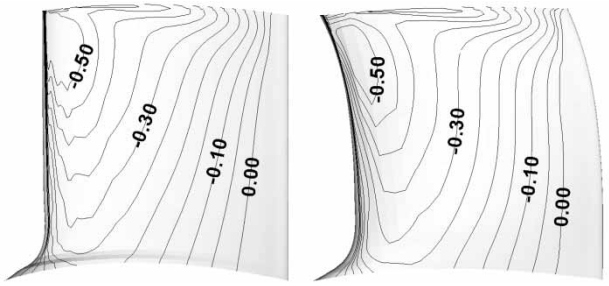

Fig. 11 Distribution of static pressure coefficient C_{p} on the SS Left: USK, right: FSK

and PS phenomena can be detected are indicated by appropriate labels. A zone of pronounced suction effect can be observed upstream of the SS of the near-tip region of FSK, indicated by increased axial velocity and counter-swirl compared with USK. Upstream of the PS of FSK, locally reduced axial velocity and increased swirl appear, compared with USK. Pitchwise-averaging points out that $\hat{\varphi}_1$ (Fig. 9) and the Euler work are higher for FSK near the tip at the rotor inlet. This is suggested also by the generally increased ψ_{id} and φ data near the FSK LE in Fig. 13. The reason for the above-mentioned is that the near-tip part of the forward-skewed blade protrudes into the upstream relative flow field, and carries out work in advance compared to the blade sections at lower radii. According to the conservation of mass at the prescribed design flowrate, increase of inlet axial velocity near the tip results in the reduction of inlet axial velocity at lower radii of FSK, as was already indicated in Fig. 9. The reduced axial velocity results in increased flow incidence angle, manifesting itself in increased lift, i.e. increased depression and overpressure on the SS and PS, respectively. This is illustrated in the C_{p}

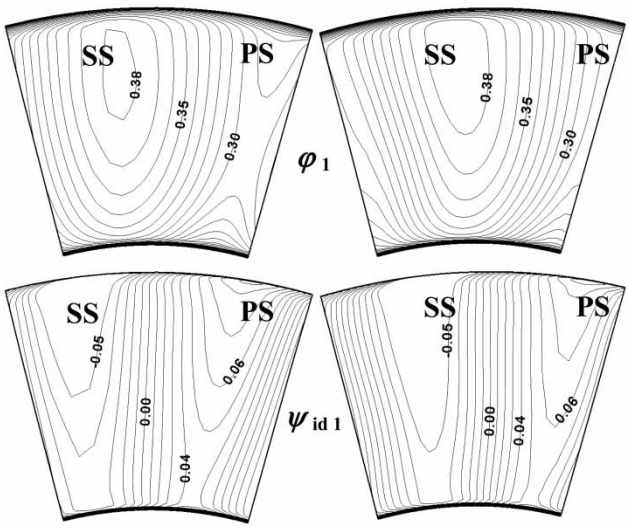

Fig. 12 Inlet flow maps. Left column: USK, right column: FSK

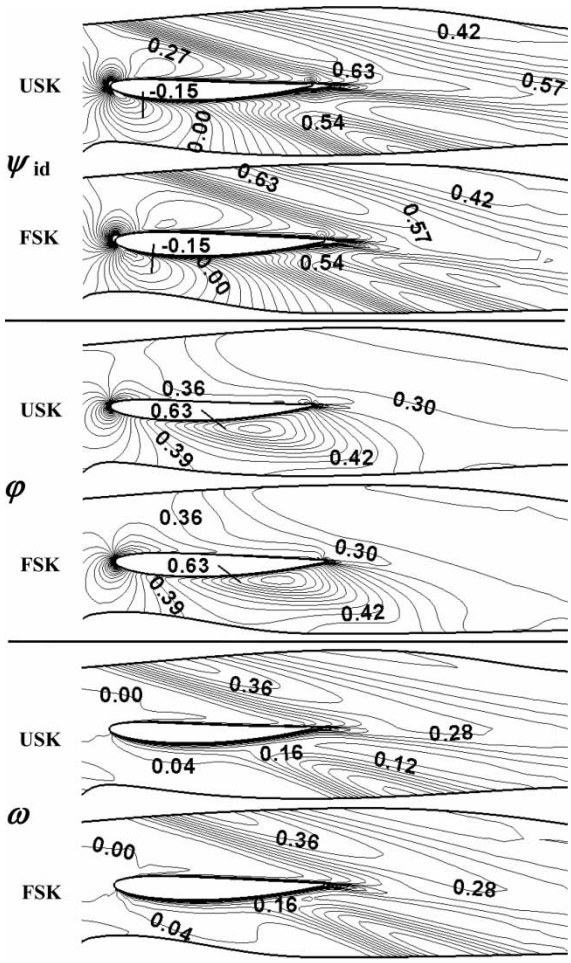

Fig. 13 Flow characteristics at 90 per cent span

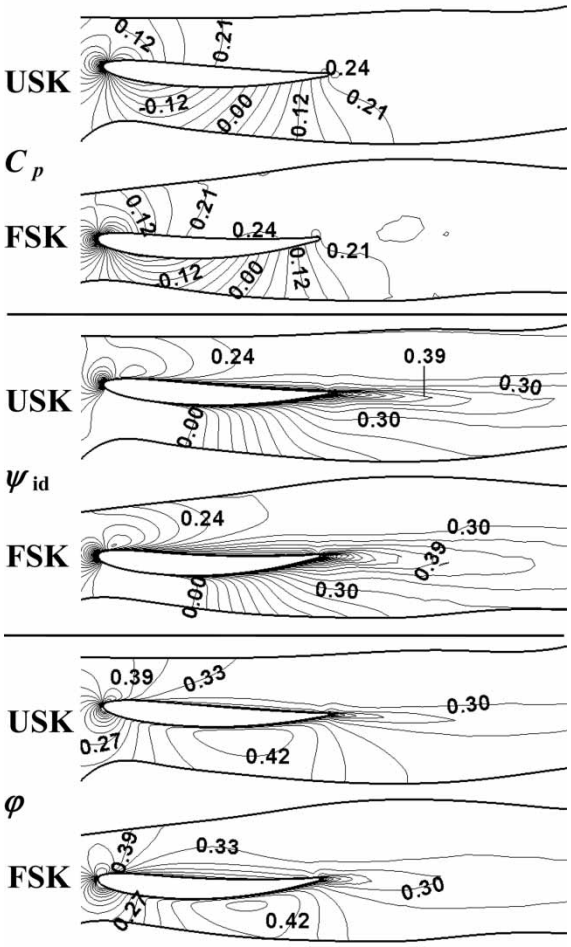

Fig. 14 Flow characteristics at 20 per cent span

plots of Fig. 14. As equation (2) suggests, the higher lift being valid for FSK at lower radii potentially leads to increased Euler work and blade section performance. Indeed, as Fig. 14 indicates, FSK performs higher ideal total pressure rise and axial velocity at lower radii, compared with USK, as was suggested already in Fig. 9.

Figure 13 shows increased loss on the SS of FSK near the tip, for the following presumed reason. Circumferential FSK results in positive sweep [**6**] near the tip, with leakage loss-reducing effects anticipated, but inevitably also in negative dihedral, i.e. acute angle between the suction surface and the casing wall. As presumed on the basis of reference [**6**], negative dihedral results in increased near-tip and leakage losses. The unfavourable effect of negative dihedral appears to dominate over the favourable effect of positive sweep from the viewpoint of losses near the tip, although the tip sweep angle is considerably larger than the tip dihedral angle (approximately 22° and 13°, respectively).

As the ω_2 plots in Fig. 10 suggest, blade sections of FSK away from the tip also have increased loss on the SS. This is mainly due to the increased flow incidence angle and the resultant higher adverse pressure gradient. The increase of losses further from the endwalls in a rotor of forward-swept tip was also discussed in reference [**11**] to the unfavourable conditions in the SS boundary layer.

6 SUMMARY AND CONCLUSIONS

Comparative CFD studies have been carried out on two rotors – USK and FSK – at the design flow rate, in order to investigate the aerodynamic effects of CVD and circumferential FSK, without geometrical correction of the elemental blade cascades of the skewed blading. Preliminary studies were published in reference [**23**]. The results are summarized as follows.

1. The studies indicated that the circumferentially forward-skewed blade tip carries out work on the incoming fluid in advance compared with the blade sections at lower radii, due to its protrusion into the upstream relative flow field. This results in increased and decreased inlet axial velocities near the tip and at lower radii, respectively.

2. The decreased axial velocity at lower radii leads to increased incidence, lift, and blade performance. Such uploading below midspan, coupled with unloading above midspan due to sweep, reduces the spanwise gradient of Euler work. Consequently, the blade circulation and axial velocity distribution prescribed along the span by the CVD concept tends towards that of a free vortex flow pattern. This results in the decrease of global ideal total pressure rise.
3. Increased total pressure loss was found along the dominant portion of the span of FSK. This was dedicated to (a) the negative dihedral near the tip, always incorporated by circumferential FSK, and (b) predominantly due to the off-design cascade conditions at lower radii, i.e. increased flow incidence due to the tip forward effect, and the related higher SS adverse pressure gradients. Due to the reduced global ideal total pressure rise and increased losses, the global total pressure rise and total efficiency of FSK were found to be reduced compared with the USK rotor.
4. For rotors of CVD, the radial outward flow on the SS is intensified in comparison with free vortex rotors, due to the vortices shed from the TE in accordance with the spanwise increasing blade circulation. This suggests that in CVD bladings, the SS boundary layer fluid has increased inclination to migrate outward and to accumulate near the tip. As the present studies indicated, forward sweep attenuates the radial outward flow on the SS. This yields that the application of forward sweep for potential reduction of near-tip loss is especially welcome for CVD rotors.
5. The present study, supplemented with literature data cited in the introduction, suggests that applicability of *ad hoc* blade stacking techniques is doubtful in the achievement of efficiency gain and prescribed performance at the design flow rate. Instead, application of reliable CFD-based design systems [**13**] is recommended for systematic consideration and control of both load- and loss-modifying effects due to non-radial blade stacking.

ACKNOWLEDGEMENTS

This work has been supported by the Hungarian National Fund for Science and Research under contracts No. OTKA T 043493 and K63704, and, on the behalf of Cs. Horváth, out of the József Öveges Program HEF_06_3 (BMEGPK06). Gratitude is expressed to Prof László Fenyvesi and Mr József Deákvári, Hungarian IAE, Gödöllő, for contributing to the measurements, and to Mr Lóránt Farkas, Szellőző Művek Kft. (Ventilation Works Ltd), for consultation.

REFERENCES

1 **Gallimore, S. J., Bolger, J. J., Cumpsty, N. A., Taylor, M. J., Wright, P. I.,** and **Place, J. M. M.** The use of sweep and dihedral in multistage axial flow compressor blading – parts I and II. *ASME, J. Turbomach.*, 2002, **124**, 521–541.

2 **Vad, J.** and **Bencze, F.** Three-dimensional flow in axial flow fans of non-free vortex design. *Int. J. Heat Fluid Flow*, 1998, **19**, 601–607.

3 **Corsini, A.** and **Rispoli, F.** Using sweep to extend the stall-free operational range in axial fan rotors. *Proc. Instn Mech. Engrs, Part A: J. Power and Energy*, 2004, **218**, 129–139.

4 **Meixner, H. U.** *Vergleichende LDA-Messungen an ungesichelten und gesichelten Axialventilatoren*. Dissertation Universität Karlsruhe, VDI-Verlag, Reihe 7: Strömungstechnik, No. 266, Düsseldorf, 1995.

5 **Lakshminarayana, B.** *Fluid dynamics and heat transfer of turbomachinery*, 1996 (John Wiley & Sons, Inc., New York, USA).

6 **Clemen, C.** and **Stark, U.** Compressor blades with sweep and dihedral: a parameter study. In Proceedings of 5th European Conference on Turbomachinery Fluid Dynamics and Thermodynamics, Prague, 2003, pp. 151–161.

7 **Beiler, M. G.** *Untersuchung der dreidimensionalen Strömung durch Axialventilatoren mit gekrümmten Schaufeln*. Doctoral Dissertation, Universität-GH-Siegen, VDI Verlag Düsseldorf, Reihe 7: Strömungstechnik, Nr. 298, 1996.

8 **Beiler, M. G.** and **Carolus, T. H.** Computation and measurement of the flow in axial flow fans with skewed blades. *ASME, J. Turbomach.*, 1999, **121**, 59–66.

9 **Yamaguchi, N., Tominaga, T., Hattori, S.,** and **Mitsuhashi, T.** Secondary-loss reduction by forward-skewing of axial compressor rotor blading. In Proceedings of Yokohama International Gas Turbine Congress, Yokohama, 1991, pp. II.61–II.68.

10 **Rohkamm, H., Wulff, D., Kosyna, G., Saathoff, H., Stark, U., Gümmer, V., Swoboda, M.,** and **Goller, M.** The impact of rotor tip sweep on the three-dimensional flow in a highly-loaded single-stage low-speed axial compressor: part II – test facility and experimental results. In 5th European Conference on Turbomachinery Fluid Dynamics and Thermodynamics, Prague, 2003, pp. 175–185.

11 **Clemen, C., Gümmer, V., Goller, M., Rohkamm, H., Stark, U.,** and **Saathoff, H.** Tip-aerodynamics of forward-swept rotor blades in a highly-loaded single-stage axial-flow low-speed compressor. In 10th International Symposium on Transport Phenomena and Dynamics of Rotating Machinery (ISROMAC10), Honolulu, 2004, paper no. 027, available in CD-ROM.

12 **Vad, J., Kwedikha, A. R. A.,** and **Jaberg, H.** Effects of blade sweep on the performance characteristics of axial flow turbomachinery rotors. *Proc. IMechE, Part A: J. Power and Energy*, 2006, **220**, 737–751.

13 **Jang, C.-M., Samad, A.,** and **Kim, K.-Y.** Optimal design of swept, leaned and skewed blades in a transonic axial compressor. ASME paper GT2006-90384, 2006.

14 **Vad, J., Kwedikha, A. R. A.,** and **Jaberg, H.** Influence of blade sweep on the energetic behavior of axial flow turbomachinery rotors at design flow rate. ASME paper GT2004-53544, 2004.

15 Vad, J. Analytical modeling of radial fluid migration in the boundary layer of axial flow turbomachinery blades. ASME paper GT2006-90523, 2006.

16 Govardhan, M., Krishna Kumar, O. G., and **Sitaram, N.** Computational study of the effect of sweep on the performance and flow field in an axial flow compressor rotor. *Proc. IMechE, Part A: J. Power and Energy*, 2007, **221**, 315–329.

17 Wallis, R. A. *Axial flow fans and ducts*, 1983 (John Wiley & Sons, New York).

18 *Fluent 6.2.16 user's guide*, 2004 (Fluent Inc., Lebanon, NH, USA).

19 Benini, E. and **Biollo, R.** On the aerodynamics of swept and leaned transonic compressor rotors. ASME paper GT2006-90547, 2006.

20 Launder, B. E. and **Spalding, D. B.** *Lectures in mathematical models of turbulence*, 1972 (Academic Press, London).

21 Kader, B. Temperature and concentration profiles in fully turbulent boundary layers. *Int. J. Heat Mass Transf.*, 1993, **24**, 1541–1544.

22 Wu, Y., Chu, W., Lu, X., and **Zhu, J.** Behavior of tip leakage flow in an axial compressor rotor. ASME paper GT2006-90399, 2006.

23 Vad, J., Kwedikha, A. R. A., and **Horváth, Cs.** Combined effects of controlled vortex design and forward blade skew on the three-dimensional flow in axial flow rotors. In Conference on Modelling Fluid Flow (CMFF'06), Budapest, 2006, pp. 1139–1146.

APPENDIX 1

Notation

c	blade chord
C_L	blade lift coefficient
C_p	local static pressure coefficient $=(p-\bar{p}_1)/(\rho u_{ref}^2/2)$
d	diameter
M	exponent in the design power law, equation (1)
n	rotor speed
N	rotor blade count
p	static pressure
r	radius $= d/2$
R	dimensionless radius $= r/r_t$
s	blade spacing (blade pitch) $= d\pi/N$
S	blade span $= (d_t - d_h)/2$
t	rotor tip clearance
u_{ref}	reference velocity $= d_t \pi n$
U	relative standard experimental uncertainty
v	flow velocity in the absolute frame of reference
w_∞	relative free-stream velocity
y^+	wall normal cell size (in wall units)
Δp_t	local total pressure rise
η	global total efficiency
η^*	overall efficiency
ν	hub-to-tip ratio $= d_h/d_t$
ρ	fluid density
σ	fraction of span (radial distance from the hub divided by S)
τ	relative tip clearance $= t/S$
φ	local axial flow coefficient $= v_x/u_{ref}$
φ_r	local radial flow coefficient $= v_r/u_{ref}$
Φ	global flow coefficient (annulus area-averaged axial velocity divided by u_{ref})
Ψ	global total pressure coefficient (annulus mass-averaged total pressure rise divided by $\rho u_{ref}{}^2/2$)
ψ	local total pressure rise coefficient $= \Delta p_t/(\rho u_{ref}{}^2/2)$
ψ_{id}	local ideal total pressure rise coefficient $= \Delta p_{tid}/(\rho u_{ref}^2/2) = 2Rv_u/u_{ref}$ (from the Euler equation of turbomachines, considering swirl-free inlet far upstream)
ω	total pressure loss coefficient $= \psi_{id} - \psi$

Subscripts and superscripts

CFD	based on CFD data
D	design; at the design flow rate
FSK	circumferentially forward-skewed blading
h	hub
id	ideal (inviscid)
M	based on measurement data
r	radial coordinate
t	blade tip
u	tangential coordinate
USK	unskewed blading
x	axial coordinate
1	rotor inlet plane
2	rotor exit plane
ˆ	pitchwise averaged value
–	passage-averaged value

APPENDIX 2

Calculation of approximate theoretical spanwise distributions of flow characteristics

Pitchwise averaged quantities are considered herein. The superscript ˆ has been omitted for simplicity.

At a given radius, the total pressure rise realized by the rotor is

$$\Delta p_t = \eta \Delta p_{t\,id} = p_{t2} - p_{t1} = \left(p_2 + \rho\frac{v_2^2}{2}\right) - \left(p_1 + \rho\frac{v_1^2}{2}\right) \quad (3)$$

The following simplifying assumptions are taken.

1. The flow is incompressible, i.e. $\rho =$ constant.
2. Although the local total efficiency in equation (3) varies along the span, it is assumed to be constant farther from the endwalls at the design flowrate, on the basis of measurement data in [**12**].
3. The inlet swirl is neglected, i.e. $v_{ul} = 0$, and the streamlines are parallel upstream of the rotor, i.e. the normal component of Euler equation in the natural coordinate system reads $p_1(r) =$ constant.
4. The radial velocity components are neglected, i.e. $v_1^2 = v_{x1}^2$ and $v_2^2 = v_{x2}^2 + v_{u2}^2$.

Taking the radial derivative of equation (3), and applying the above simplifications, reads

$$\eta \frac{\mathrm{d}(\Delta p_{\mathrm{t\,id}})}{\mathrm{d}r} = \frac{\mathrm{d}p_2}{\mathrm{d}r} + \rho v_{x2} \frac{\mathrm{d}v_{x2}}{\mathrm{d}r} + \rho v_{u2} \frac{\mathrm{d}v_{u2}}{\mathrm{d}r} - \rho v_{x1} \frac{\mathrm{d}v_{x1}}{\mathrm{d}r} \tag{4}$$

The Euler equation of turbomachines for swirl-free inlet is as follows

$$\Delta p_{\mathrm{t\,id}} = \rho u v_{\mathrm{u2}} \tag{5}$$

According to the Euler equation, $\mathrm{d}p_2/\mathrm{d}r$ is expressed as

$$\frac{\mathrm{d}p_2}{\mathrm{d}r} = \rho \frac{v_{\mathrm{u2}}^2}{r} \tag{6}$$

Substituting equations (5) and (6) to equation (4), rearranging, and putting into a dimensionless form reads

$$\frac{\mathrm{d}\psi_{\mathrm{id\,2}}}{\mathrm{d}R} \left(\eta - \frac{\psi_{\mathrm{id\,2}}}{2R^2} \right) = 2 \left(\varphi_2 \frac{\mathrm{d}\varphi_2}{\mathrm{d}R} - \varphi_1 \frac{\mathrm{d}\varphi_1}{\mathrm{d}R} \right) \tag{7}$$

When determining the theoretical $\psi_{\mathrm{id\,2}}(R)$ distributions in Fig. 7, the measured as well as the computed $\varphi_1(R)$ and $\varphi_2(R)$ distributions were approximated as linear functions from 20 to 80 per cent span, using the least squares method. This provided for local approximate data of φ_1, $\mathrm{d}\varphi_1/\mathrm{d}R$, φ_2, and $\mathrm{d}\varphi_2/\mathrm{d}R$ to be substituted into equation (7). The differential equation (7) was solved for $\psi_{\mathrm{id\,2}}(R)$ numerically for the spanwise region of axial velocity linearization, retaining the computed $\psi_{\mathrm{id\,2}}$ data at midspan as boundary condition. For determination of the theoretical $\varphi_2(R)$ distributions in Fig. 9, the $\varphi_1(R)$ and $\psi_{\mathrm{id\,2}}(R)$ distributions were linearized, and equation (7) was solved numerically, retaining the computed φ_2 data at midspan as boundary condition. $\eta = 0.90$ was set for each case as representative value, based on reference [**12**].

The $\psi_{\mathrm{id2\,D}}(R)$ and $\varphi_{\mathrm{2\,D}}(R)$ distributions shown in Fig. 9 were determined on the basis of equations (1) and (7), but assuming uniform axial inlet condition, applying empirical corrections considering the spanwise change of efficiency and the blockage due to the annulus wall boundary layers, and taking the prescribed Φ_{D} and Ψ_{D} data as integral conditions.